Non Local Model Free Denoising Algorithm for Single and Multi-Channel SAR Data

Hossein Aghababaei, *Senior Member, IEEE*, Giampaolo Ferraioli, *Senior Member, IEEE*, Sergio Vitale, *Student Member, IEEE*, Roghayeh Zamani, Gilda Schirinzi, *Senior Member, IEEE*, Vito Pascazio, *Senior Member, IEEE*

***Abstract*—Among the large number of Synthetic Aperture Radar (SAR) image despeckling approaches existing in literature, Non-Local (NL) filters have received a desirable boost. However, often NL approaches define the similarity critirion based on model assumptions, such as a fully developed speckle model. This assumption may not be verified in high-resolution images of urban environments. To address this issue, a stand-alone model-free despeckling framework is proposed in this paper. The presented approach provides a generic framework for denoising a variety of SAR products, from a single intensity/amplitude image to polarimetric and interferometric SAR data. In particular, the method is based on the empirical distributional similarity between the patch containing the pixel to be recovered and the patch containing a similar candidate pixel. To decide whether the patches follow a similar distribution, the Kolmogorov-Smirnov test is adapted. Finally, the restoration process aggregates the selected similar pixels based on their relative importance derived from their distribution similarities. To mitigate the blurring effect and preserve the resolution, the inhomogeneity of the ratio image is used to perform the bias reduction step. The designed generic despeckling filter was tested on different products of SAR data. The results show that the method proves to be an unbiased restoration approach and is able to preserve structures and textures. It works fully automatically and efficiently with single and multi-look (and multi-channel) images.**

***Index Terms*—Despeckling, interferometry, non-local, polarimetry, ratio image, synthetic aperture radar (SAR)**

I. Introduction

SPECKLE reduction in Synthetic Aperture Radar (SAR) images is a challenging task that, if not correctly handled, can impair SAR image based applications. The speckle phenomenon arises from the random constructive and destructive interference of scattered signals within the resolution cell: the overall consequence on a SAR image is the appearance of bright (constructive interference) and dark (destructive interference) spots in the images [1]. In other words: In homogeneous areas, adjacent resolution cells can have completely different backscattering values because the elementary scatterers are randomly arranged within the resolution cells. This effect makes SAR images difficult to interpret and difficult to use for various applications [2].

The problem of removing or mitigating speckle in SAR domain, commonly known as despeckling, has been studied for about forty years. Based on the idea underlying the filter, several classifications of the available developed despeckling filters can be considered. A commonly adopted classification divides the approaches into two categories: 1) single-image and 2) multi-channel. In the first class, the goal of the filters is to remove speckle from a single amplitude/intensity SAR image. Within this branch, the algorithms have been developed in two different domains: spatial [3], [4], [5] and transformed one [6], [7]. For an in-depth analysis of single-channel algorithms, see [8], [9], where the most popular and effective approaches are presented, analyzed and compared.

The other family of filters, the multi-channel ones, have the aim of filtering together multiple available images of the same scene. This can be done in the case of multi-temporal images (*i.e.* images of the scene taken at different times) [10], [11], or in the case of polarimetric images (*i.e.* images of the same scene acquired at the same time but with different polarizations) [12], [13], [14]. These images are also generally referred to as multi-channel images, without specifying whether they are multi-temporal, multi-polarimetric or both.

Apparently single image algorithms could be extended to the multi-channel case. However, with a simple extension, they would not be able to take into account the possible correlation between the available images and may have computational problems due to the increase in dimensionality [15]. The multi-channel algorithms usually rely on the estimation of the complex covariance matrix containing all the properties of the images (amplitudes, phases and the correlation between the channels). However, such methods usually assume an important hypothesis about the nature of the speckle: It is considered fully developed. The latter is not always the case in heterogeneous areas and is not always satisfied in extremely heterogeneous scenarios (such as urban areas) characterized by the presence of dominant scatterers [16], [17].

A special class of despeckling algorithms is that of non-local (NL) filters. Initially developed for single images, [18], [19], [20], they were then developed to work with multi-channel data [21], [22], [23], [24], [25]. Based on exploiting the similarity between patches (pixel clusters), they provide very accurate results both in removing noise and preserving details. In the last decade, several NL despeckling algorithms have appeared in the literature. The main difference between

H. Aghababaei is with Department of Earth Observation Science,University of Twente Faculty of Geo-Information Science and Earth Observation, Twente, Netherlands

G. Ferraioli is with Dipartimento di Scienze e Tecnologie, Università degli Studi di Napoli "Parthenope", Naples, Italy and with the National Inter-University Consortium for Telecommunications - CNIT, Naples, Italy.

S. Vitale and R. Zamani are with Dipartimento di Scienze e Tecnologie, Università degli Studi di Napoli "Parthenope", Naples, Italy.

V. Pascazio and G. Schirinzi are with Dipartimento di Ingegneria, Università degli Studi di Napoli "Parthenope", Naples, Italy and with the National Inter-University Consortium for Telecommunications - CNIT, Naples, Italy.

the approaches lies in the definition of the similarity criterion and in the function used to merge similar pixels.

In this paper, a model-free NL based algorithm able to work with multi-channel images is presented. The proposed methodology allows the processing and restoring a variety of SAR images, from a single image to polarimetric and interferometric images. The presented framework is based on the estimation of two similarity criteria, one of which is obtained by directly comparing the distributions of the patches, while the other compares the distribution of ratio patches [26]. Regarding the second criterion, if two speckles have the same underlying texture (noise-free component), their ratio is the ratio between two pure speckles (*i.e.*, with the same statistical distribution). Thus, both the ratio and the inverse ratio are expected to follow the same distribution. This model-free approach allows to avoid mischaracterization of the speckle model: the algorithm will not force a statistical hypothesis for all possible scenarios: homogeneous, heterogeneous, extremely heterogeneous areas or mixed [27]. At the same time, the algorithm benefits from the NL paradigm and provides effective results in terms of both speckle reduction and detail preservation.

This paper is organized as follows. Section II introduces the speckle model and the problem formulation. Section III surveys the work that inspired the proposed method. The details of the proposed despeckling framework are presented in Section IV. The experimental results obtained by evaluating several datasets are given in Section V, while Section VI is devoted to the conclusions.

II. Speckle Fluctuation in SAR Images and Problem Definition

Speckle is a granular disturbance, commonly modeled as multiplicative noise, that strongly impairs SAR images. In principle, the received complex signal $y(p)$ in each resolution cell p is the result of some constructive and destructive interference between waves reflected from elementary scatterers within the cell. If the resolution cell contains distributed scatterers, *i.e.*, multiple scatterers, none of which provides a much stronger reflected signal than the others, then the received signal is theoretically the sum of several backscattered waves [8]. In such a case, when a large number of scatterers are present in the cell, the received backscattering signal will have a uniform phase distribution if the range distance and spatial resolution are much larger than the wavelength used. In fact, due to the random arrangement of the scatterers, the distance between the scatterers and the radar is random. Therefore, the phases of the paths are different and randomly varying. Typically, when $y(p)$ possesses these properties, speckle is termed as *fully developed* [28]. In general, the single look complex (SLC) SAR image is noisy due to the constructive/destructive combination effects described earlier, and thus all parameters derived from the SLC image are affected by the strong signal-dependent variance.

In multi-channel (either polarimetric or interferometric) data, where there is a stack of N co-registered SLC images, the data in each resolution cell p can be represented by a N-dimensional complex scattering vector as $\mathbf{y}(p) = [y_1(p)\ y_2(p)...y_N(p)]^T \in \mathbb{C}^{N\times 1}$, where ^{T} is the transpose operator. In such a case, the probability density function (pdf) of the scattering vector is the circular complex Gaussian one [1]:

$$f_{\mathbf{y}}(\mathbf{y}|\mathbf{\Sigma}) = \frac{1}{\pi^N|\mathbf{\Sigma}|}\exp(-\mathbf{y}^\dagger\mathbf{\Sigma}^{-1}\mathbf{y}) \tag{1}$$

where $\mathbf{\Sigma} = E\{\mathbf{y}\mathbf{y}^\dagger\} \in \mathbb{C}^{N\times N}$ is the complex data covariance matrix. In Eq. (1), the dependence of scattering vector $\mathbf{y}$ and $\mathbf{\Sigma}$ on the pixel coordinate p is not explicitly stated for the sake of notational simplicity. In addition, the operators †, $|.|$ and E denote the Hermitian transpose, determinant, and mathematical expectation, respectively.

In Eq. (1), the true covariance matrix $\mathbf{\Sigma}$ is unknown due to the unavailability of the signal realizations. However, it is straightforward to approximate it by the sample covariance matrix ($\hat{\mathbf{R}}$) through the maximum likelihood estimation (MLE) of L pixels with similar scattering vectors. In general, when $L \geq N$, then $\hat{\mathbf{R}}$ is a full-rank matrix and can be described by the complex Wishart distribution given by $\hat{\mathbf{R}} \sim \mathcal{W}_{\hat{\mathbf{R}}}(\mathbf{\Sigma}, N, L)$:

$$f_{\hat{\mathbf{R}}}(\hat{\mathbf{R}}|\mathbf{\Sigma}) = \frac{L^{NL}|\hat{\mathbf{R}}|^{L-N}}{\Gamma_N(L)|\Sigma|^L}\exp(-L\cdot\mathrm{Tr}(\mathbf{\Sigma}^{-1}\hat{\mathbf{R}})) \tag{2}$$

where $\mathrm{Tr}(.)$ denotes the trace operator, and $\Gamma_N(L) = \pi^{N(N-2)/2}\prod_{n=1}^{N}\Gamma(L-n+1)$, in which $\Gamma(.)$ is the standard Euler gamma function.

The given models in Eqs. (1,2) rely on the fully developed speckle assumption and are the basis of several developed despeckling filters in the literature [29], [30]. For example, the identification and selection of similar pixels based on the fully developed speckle model was performed in [26] for denoising single-channel amplitude images or in [18], [21], [30] for estimating the sample covariance matrix with multi-channel data.

However, as mentioned earlier, the Goodman's fully developed speckle model Eqs. (1,2) may not be verified in high-resolution images of urban environments, where persistent scatterers and not fully developed speckle often occur [16], [17], [27]. Thus, in such regions, if the similarity is computed based on the particular Goodman's speckle model, the efficiency of the despeckling filter may be severely compromised. To overcome this problem, this paper proposes a model-free approach to compare noisy pixels and find the similarity without relying on the Goodman's assumption, which is sorely lacked in the literature. As a basis for our development, two standard filtering techniques are discussed in the next section, while section IV introduces the proposed model-free despeckling filter.

III. Review on NL model-based Approaches

In this Section a short review of NL model-based filtering techniques is presented. The review is limited to the two papers [21], [26] that inspired the proposed one. An interesting revision of NL methods for despekling can be found in [29]. Both the considered methods exploit the NL paradigm. The first algorithm is NoLAnD, a despeckling algorithm, able to work on single images based on the use of the ratio patch for

This article has been accepted for publication in a future issue of this journal, but has not been fully edited. Content may change prior to final publication. Citation information: DOI 10.1109/TGRS.2021.3127109, IEEE Transactions on Geoscience and Remote Sensing

defining the similarity criterion. The second one is NLSAR, whose aim is to provide a general framework for processing and restoring single and multi-channel images exploiting the covariance matrix. Before introducing the two approaches, the NL paradigm is briefly recalled.

A. Non-local filtering framework

The NL framework is based on finding non-local neighbors of the target pixel p to be filtered, within a search window of a given size, that have a statistical similarity to the pixel p. Typically, the pixel p is located in the center of the search window (see Fig. 1). A pixel q in the search window is assumed to be similar to pixel p if their patches or local neighbors surrounding the two pixels are similar. The patches have the same shape and dimension centered on pixels p and q (Fig. 1). Therefore, the similarity for two pixels is discerned by comparing the information of their patches. Once the similarities of all pixels in the search window are estimated, the aggregation of pixels is performed using the weighted maximum likelihood approach, while the weight value is generally estimated from the degree of similarity.

B. The ratio based filtering

In the context of model-based filtering, a non-local technique, called NOLAND, was proposed in reference [26] to denoise a single amplitude image. Let us represent the noisy amplitude signal $A(p)$ as a product of the deterministic $X(p)$ and the noise $S(p)$ terms:

$$A(p) = X(p) \cdot S(p) \tag{3}$$

The noise term in (3) follows a square root gamma distribution as [8]:

$$f_S(s) = \frac{2L^L}{\Gamma(L)} s^{2L-1} \cdot \exp\left(-Ls^2\right) \cdot u(s) \tag{4}$$

where $\Gamma()$ is the Gamma function and $u()$ is the unitary step function. In case of $L = 1$, i.e. SLC image, the distribution becomes a Rayleigh pdf, with parameter $\sigma = 1/\sqrt{2}$.

For two similar pixels p and q whose deterministic or noise-free components are equal, *i.e.* $X(p) = X(q)$, the ratio between their amplitudes is equal to the ratio between their speckle components. *i.e.* $v = A(p)/A(q) = S(p)/S(q)$. Moreover, based on Goodman's model the given ratio between two fully developed speckle noises can be modelled according to the following probability distribution function [31]

$$f_V(v) = \frac{2\Gamma(2L)v^{2L-1}}{\Gamma(L)^2(v^2+1)^{2L}} \tag{5}$$

Indeed, NOLAND is based on the idea of generating the ratio patch between the patch P containing the pixel p to be restored and the patch Q containing a candidate similar pixel q (see patches P and Q in Fig. 1). When the deterministic parts of two patches are equal, their corresponding ratio patch is expected to follow the statistical distribution model given in Eq. (5). On the contrary, when the deterministic parts of the patches are different, the distribution of the ratio patch deviates from the model in Eq. (5). Therefore, the similarity

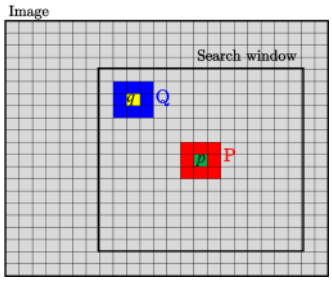

Fig. 1. Representation of the non-local framework

of the two patches is measured by the Kolmogorov-Smirnov (KS) distance:

$$\delta(p,q) = \max_v |F_V(v) - E_{V_{PQ}}(v)| \tag{6}$$

where F_V is the cumulative distribution function of f_V, and $E_{V_{PQ}}$ is the empirical cumulative distribution function (ECDF) of the ratio patch. Given the vectors collecting the K pixels within the considered patch

$$\begin{aligned} \mathbf{a}_P &= [A(p_1)A(p_2) \ldots\ldots A(p_K)] \\ \mathbf{a}_Q &= [A(q_1)A(q_2) \ldots\ldots A(q_K)] \end{aligned} \tag{7}$$

the ratio patch can be generated as

$$\mathbf{v} = \left[\frac{A(p_1)}{A(q_1)} \; \frac{A(p_2)}{A(q_2)} \ldots\ldots \frac{A(p_K)}{A(q_K)}\right] \tag{8}$$

It is being understood that the similarity criterion in Eq. (6) is based on the fully developed speckle model, but the assumption for the urban and layover areas may not be valid. In such a case, when multiple scatterers are superimposed in a single resolution cell, the pdf of the noise ratio may not be given by the model in Eq. (5). Therefore, the performance of NOLAND in the high-resolution image of urban areas may be affected.

C. The unified NLSAR approach

NLSAR is a unified patch-based technique for despeckling of single and multi-channel SAR data [21]. The technique is a model-based approach where the similarity criterion is based on the model assumption in Eq. (1). In the context of NLSAR, the information of each patch is represented in terms of *pre-estimated* sample covariance matrix ($\hat{\mathbf{C}}$) computed using a finite number of neighborhood pixels. Among the various approaches for comparing the pre-estimated covariance matrices [30], NLSAR uses the generalized likelihood ration (GLR) based measure, which shows the best performance and satisfies some invariance properties [21].

$$\delta_{GLR}(\hat{\mathbf{C}}(p), \hat{\mathbf{C}}(q)) = \frac{|\hat{\mathbf{C}}(p)|^L |\hat{\mathbf{C}}(q)|^L}{|\frac{1}{2}\left(\hat{\mathbf{C}}(p) + \hat{\mathbf{C}}(q)\right)|^{2L}} \tag{9}$$

The criterion in Eq. (9) has been shown to be an efficient method with single and multi-channel data. However, similar to NOLAND, the efficiency of NLSAR relies on the assumption of a fully developed speckle model. In particular, in extremely heterogeneous regions, the scattering vector may

not follow the given model in Eq. (1). In such a case, since the likelihood of the sample covariance matrix differs from the Wishart distribution, the probability loss of the estimate in Eq. (9) is not negligible.

Apart from the problems mentioned above, both NLSAR and NOLAND provide effective results. In this paper, we consider these two techniques as the basis for developing our proposed approach, understanding and solving their limitations.

IV. THE PROPOSED GENERIC MODEL-FREE FRAMEWORK

In this section, we describe the proposed generic model-free framework for NL denoising SAR images. The main aspect of the method relates to the use of a model-free similarity criterion for patch comparison. The general scheme of the method is explained in the following. However, to facilitate the explanations, the definition of the similarity measures is introduced separately for single and multi-channel datasets.

A. Step 1: Definition of the similarity criteria

A-1) Similarity criteria for single channel SAR image

Having a single channel SAR image, the patches P and Q can be represented with the vectors collecting the amplitudes or intensities of K related pixels, *i.e.* $\mathbf{a}_P$ and $\mathbf{a}_Q$ defined in (7).

In general, the vectors $\mathbf{a}_P$ and $\mathbf{a}_Q$ may follow the random model for the distributed targets where there is no dominant scatterer; while for a point-like scatterer they are K-dimensional deterministic vectors. However, without worrying about the distribution of the patches, the given patches P and Q can be compared. In particular, the *Null hypothesis* that two patches are similar can be confirmed if:

- The vectors $\mathbf{a}_P$ and $\mathbf{a}_Q$ are drawn from the same statistical distribution.
- The ratio vector $\mathbf{v}$ of (8) and its element-wise reciprocal ($\mathbf{v}.^{-1}$) are drawn from same statistical distribution.

It is being understood that if the deterministic parts of noisy patches are equal, then both $\mathbf{v}$ and $\mathbf{v}.^{-1}$ correspond to the noise ratio (since both $S(p)/S(q)$ and $S(q)/S(p)$ represent the speckle ratio). Therefore, it is expected that their distributions come from the same model. In general, comparing the distribution of $\mathbf{v}$ with its reciprocal distribution (instead of the well-known model of Eq. (5)) allows us to go beyond the limits that might be imposed by the model assumption. It is readily understandable that in the *Alternative hypothesis* the previous statements are not valid and neither $\mathbf{a}_P$ and $\mathbf{a}_Q$ nor $\mathbf{v}$ and $\mathbf{v}.^{-1}$ follow the same distributions, since the deterministic parts of the patches are different. Therefore, the proposed similarity criterion for single-channel SAR images is defined based on the distance between the distributions, which can be measured by the KS distances:

$$\begin{aligned}\delta_{\mathbf{a}}(p,q) &= \max_{y}|E_{\mathbf{a}_P}(y) - E_{\mathbf{a}_Q}(y)|\cdot K_{mod}\\ \delta_{\mathbf{v}}(p,q) &= \max_{v}|E_{\mathbf{v}_{PQ}}(v) - E_{\mathbf{v}_{QP}}(v)|\cdot K_{mod}\end{aligned} \tag{10}$$

where the term $K_{mod} = \left(\sqrt{K} + 0.12 + \frac{0.11}{\sqrt{K}}\right)$ allows to avoid the dependence of KS distance to the considered patch size [26], $E_{\mathbf{a}_P}$ and $E_{\mathbf{a}_Q}$ represent the ECDFs of $\mathbf{a}_P$ and $\mathbf{a}_Q$, while $E_{\mathbf{v}_{PQ}}$ and $E_{\mathbf{v}_{QP}}$ indicate the ECDFs of $\mathbf{v}$ and $\mathbf{v}.^{-1}$, respectively.

Generally, the patch-based technique may not be able to optimally restore the images with sharp edges. Following the idea presented in [26], the anisotropic strategy is adapted to deal with this problem. The strategy involves computing the KS distances in four main directions (horizontal, vertical, and the two main diagonals). In particular, the distances in (10) are computed four different times using patches centered in p and q, elongated on the four directions considered. After computing the distances in four directions, $\delta_{\mathbf{a}_{xx}}$ and $\delta_{\mathbf{v}_{xx}}$ with $xx = 1, 2, 3, 4$, they are merged by taking their mean value:

$$\begin{aligned}\bar{\delta}_{\mathbf{a}}(p,q) &= \left(\delta_{\mathbf{a}_1} + \delta_{\mathbf{a}_2} + \delta_{\mathbf{a}_3} + \delta_{\mathbf{a}_4}\right)/4\\ \bar{\delta}_{\mathbf{v}}(p,q) &= \left(\delta_{\mathbf{v}_1} + \delta_{\mathbf{v}_2} + \delta_{\mathbf{v}_3} + \delta_{\mathbf{v}_4}\right)/4\end{aligned} \tag{11}$$

A-2) Similarity criteria with multi-channel SAR images

In a general case, let us refer to a stack of N co-registered SLC SAR images, where the scattering vector of a pixel p is represented by $\mathbf{y}(p) \in \mathbb{C}^{N\times 1}$. It is being understood that in the case of a fully polarimetric dataset, the complex entries of $\mathbf{y}(p)$ correspond to each combination of emission/reception polarizations. According to the reciprocity theorem, the emission and reception of an electromagnetic signal with horizontal (h) - vertical (v) polarizations leads to the representation of the scattering vector as $\mathbf{y}(p) = [y_{hh}\ y_{hv}\ y_{vv}]^T \in \mathbb{C}^{3\times 1}$. Moreover, $\mathbf{y}(p)$ can meet the stack of backscattering from multi-channel images constructed by interferometric (InSAR) data or even polarimetric interferometric (PolInSAR) data modalities. The use of *pre-estimated* sample covariance matrix is a simple way to represent multi-look multi-channel information of pixels [29]. The pre-estimated covariance matrix can be calculated using L bounded neighborhood pixels as follows:

$$\hat{\mathbf{C}} = \sum_{l=1}^{L} \mathbf{y}(l)\mathbf{y}^{\dagger}(l) \tag{12}$$

It is worth recalling that when the pre- estimated covariance matrices are computed using a limited spatially adjacent pixels, and in particular when $L << N$, $\hat{\mathbf{C}}$ is a singular matrix and it may not be invertible. Therefore, the adapted technique in [21] is used to enforce the full-rank and invertible conditions to pre-estimated sample covariance matrix. In particular, the off-diagonal elements of $\hat{\mathbf{C}}$ are rescaled as $\hat{\mathbf{C}}_{i,j} = \gamma\hat{\mathbf{C}}_{i,j}$, where $\gamma^3 = min(\frac{L}{N}, 1)$, so that $\hat{\mathbf{C}}$ becomes a full-valued matrix.

Accordingly, to represent the patch information of multi-channel dataset, the defined informative vector in (7) is modified as follows:

$$\begin{aligned}\mathbf{a}_P &= \left[\mathrm{Tr}(\hat{\mathbf{C}}(p_1))\ \ \mathrm{Tr}(\hat{\mathbf{C}}(p_2))\ .....\ \ \mathrm{Tr}(\hat{\mathbf{C}}(p_K))\right]./N\\ \mathbf{a}_Q &= \left[\mathrm{Tr}(\hat{\mathbf{C}}(q_1))\ \ \mathrm{Tr}(\hat{\mathbf{C}}(q_2))\ .....\ \ \mathrm{Tr}(\hat{\mathbf{C}}(q_K))\right]./N\end{aligned} \tag{13}$$

where $\mathrm{Tr}(.)$ indicates trace operator. Needless to point out that for single-channel SAR image Eqs. (13) boil down to intensity vector in (7).

Taking into account the multiplicative characteristic of speckle (3), the fluctuation in multi-channel SAR images can

This article has been accepted for publication in a future issue of this journal, but has not been fully edited. Content may change prior to final publication. Citation information: DOI 10.1109/TGRS.2021.3127109, IEEE Transactions on Geoscience and Remote Sensing

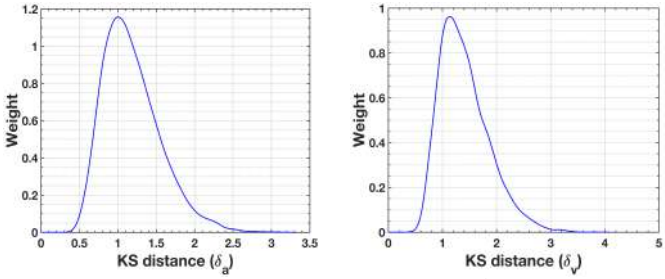

(a) $w_{\mathbf{a}}$ (b) $w_{\mathbf{v}}$

Fig. 2. Weighting functions for the proposed algorithm in case of 5-look three channels dataset.

be modeled using the following relation between sample $\hat{\mathbf{R}}$ and the true $\boldsymbol{\Sigma}$ covariance matrices, *i.e.*

$$\hat{\mathbf{R}} = \boldsymbol{\Sigma}^{\frac{1}{2}} \mathbf{S} \boldsymbol{\Sigma}^{\frac{1}{2}} \tag{14}$$

where $\mathbf{S} = E\{\mathbf{s}\mathbf{s}^{\dagger}\}$, and $\mathbf{s} = [s_1 s_2 ... s_N]^T$ indicates the speckle component of multi-channel target vector. Following the relation in (15), let define the ratio and inverse ratio matrices between two pre-estimated sample covariance matrices as:

$$\begin{aligned} \mathbf{B}_{p,q} &= \hat{\mathbf{C}}(q)^{-\frac{1}{2}}\, \hat{\mathbf{C}}(p)\, \hat{\mathbf{C}}(q)^{-\frac{1}{2}} \\ \mathbf{B}_{q,p} &= \hat{\mathbf{C}}(p)^{-\frac{1}{2}}\, \hat{\mathbf{C}}(q)\, \hat{\mathbf{C}}(p)^{-\frac{1}{2}} \end{aligned} \tag{15}$$

From (15), when the true covariance matrices of the pixels are equal, *i.e.* $\boldsymbol{\Sigma}(p) = \boldsymbol{\Sigma}(q)$, then both $\mathbf{B}_{p,q}$ and $\mathbf{B}_{q,p}$ will correspond to the ratio between speckle matrices. In such a case, it is expected that the traces of $\mathbf{B}_{p,q}$ and $\mathbf{B}_{q,p}$ follow the same distribution model. From this fact the ratio vector $\mathbf{v}$ is modified as:

$$\begin{aligned} \mathbf{v} &= [tr(\mathbf{B}_{q_1,p_1})\ tr(\mathbf{B}_{q_2,p_2})\ .....\ tr(\mathbf{B}_{q_K,p_K})]\ ./N \\ \mathbf{v}.^{-1} &= [\mathrm{Tr}(\mathbf{B}_{p_1,q_1})\ \ \mathrm{Tr}(\mathbf{B}_{p_2,q_2})\ .....\ \ \mathrm{Tr}(\mathbf{B}_{p_K,q_K})]\ ./N \end{aligned} \tag{16}$$

Accordingly, in analogy to the single-channel denoising framework, when two patches P and Q are similar, the *Null hypothesis* cannot be disapproved if:

- The vectors $\mathbf{a}_P$ and $\mathbf{a}_Q$ in (13) are drawn from the same statistical distribution.
- The ratio and inverse ratio vectors ($\mathbf{v}$ and $\mathbf{v}.^{-1}$) in (16) are drawn from the same statistical distribution.

Giving the vectors $\mathbf{a}$ and $\mathbf{v}$, the KS distances represented in (10) can be computed. Similarly, to enrich the performance of KS measures especially for sharp edges, anisotropy is taken into account, which considers the four main directions, as in (11). Once the similarity distances $\bar{\delta}_{\mathbf{a}}(p,q)$ and $\bar{\delta}_{\mathbf{v}}(p,q)$ are computed, the next step can be performed to map the similarities into a weight function.

B. Step 2: Aggregation process

In contrast to local despeckling techniques, the non-local approaches do not essentially select neighborhood pixels, but samples that follow the same distribution within an extended neighborhood with high probability. Therefore, for a reference pixel p the extended neighborhood can be defined by a search window constructed around the pixel (see the black window in Fig. 1). Then, using the method described earlier, the similarity of each pixel in the search window to the reference pixel is computed. Once the similarity of the samples in the extended neighborhood has been computed, it is necessary to define how these samples should be aggregated to obtain a NL estimation of the restored pixel. For this aim, the weighting function must be defined according to the relative importance of each sample used in the NL estimation. Following the unsupervised framework presented in [26], in the proposed despeckling approach, the weights are derived from the probability distribution of KS distances in (10) when the null hypothesis is confirmed. The weight functions for both KS distances are shown in Fig. 2. Note that the plots represent the pdfs of the KS distances of two noisy patches whose deterministic components are equal. The pdfs were obtained with numerical simulation when $N = 3$ and $L = 5$.

From both pdfs, it can be seen that pixels with values of KS distances approximately equal to one are considered in the fusion step, while pixels belonging to patches with large or very small distances are neglected. The final weighting function for aggregating the pixels can be defined as follows:

$$w(p,q) = \sqrt{w_{\mathbf{a}}(p,q) \cdot w_{\mathbf{v}}(p,q)} \tag{17}$$

where $w_{\mathbf{a}}$ and $w_{\mathbf{v}}$ are the weight function related to KS distances $\bar{\delta}_{\mathbf{a}}$ and $\bar{\delta}_{\mathbf{v}}$, respectively (See Fig. 2).

Once the similarities are mapped into a weight values using (18), the non-local covariance matrix is computed using the weighted maximum likelihood estimator as [18], [21]:

$$\hat{\mathbf{R}}(p) = \frac{\sum_q w(p,q)\mathbf{y}(q)\mathbf{y}^{\dagger}(q)}{\sum_q w(p,q)} \tag{18}$$

It should be noted that when single-channel data is processed, $\hat{\mathbf{R}}$ and $\mathbf{y}$ boil down to the filtered and noisy amplitudes or intensities, respectively *i.e.*:

$$\hat{A}(p) = \frac{\sum_q w(p,q)A(q)}{\sum_q w(p,q)} \tag{19}$$

C. Step 3: Bias reduction process

The final step of the non-local procedure involves in bias reduction. Weighted averaging can result in overly smoothed images and spread out the bright structures whose intensities are several orders of magnitude larger than their surrounding background. To recover the bright targets, the convex combination between the NL estimate and the noisy empirical covariance matrices is performed as [21], [32]:

$$\hat{\boldsymbol{\Sigma}}(p) = \hat{\mathbf{R}}(p) + \beta \left(\hat{\mathbf{C}}(p) - \hat{\mathbf{R}}(p) \right) \tag{20}$$

where $\hat{\boldsymbol{\Sigma}}$ is denoted as the bias-reduced NL estimate of the sample covariance matrix. It can be seen that $\hat{\boldsymbol{\Sigma}}$ corresponds to $\hat{\mathbf{R}}$ and pre-estimated sample covariance matrix when β approaches zeros and one, respectively. Note that for the amplitude image case, the estimate is updated as follows:

$$\hat{A}(p) = \hat{A}(p) + \beta \left(A(p) - \hat{A}(p) \right) \tag{21}$$

The typical approach for estimating β, is presented in [21], [33], where the technique is based on the variance of the intensity in a homogeneous region equal to $\hat{A}^2/L$. Theoretically,

heterogeneity in a collection of samples increases the variance so that it is much higher than the typical value of $\hat{A}^2/L$. This concept was used in [21] to define the parameter β. The approach used in [21] enjoys the estimation of the parameter independently on each channel and without being affected by the correlations between channels in [33]. However, using this approach may lead to higher values of β in homogeneous regions. This is to be expected since the estimated variance of intensity in limited samples may not be exactly the same as $\hat{A}^2/L$. Therefore, to improve the efficiency of the bias reduction algorithm, the heterogeneity of the ratio image is considered in this paper. The proposed β is calculated using the following equation.

$$\beta = \sqrt{\beta_1 . \beta_2} \tag{22}$$

where β_1 is still the variance based estimation introduced in [21], while β_2 is computed by the heterogeneity of the ratio image. Once the sample covariance matrix is estimated in (19), the ratio matrix that representing the speckle can be computed as follows:

$$\hat{\mathbf{S}} = \hat{\mathbf{R}}^{-\frac{1}{2}} \hat{\mathbf{C}} \hat{\mathbf{R}}^{-\frac{1}{2}} \tag{23}$$

In homogeneous regions $\hat{\mathbf{S}}$ follows Wishart distribution as $\hat{\mathbf{S}} \sim \mathcal{W}_c(\mathbf{I}, N, L)$, where $\mathbf{I}$ is identity matrix [34]. It is known that the normalized trace of matrix $\hat{\mathbf{S}}$, i.e. $T_N = \mathrm{Tr}(\hat{\mathbf{S}})/N$, follows central Chi-square distribution with $2NL$ degrees of freedom, therefore the pdf of T_N can be obtained as [34], [35]:

$$f_{T_N}(t) = \frac{NL^{NL}}{N(L-1)!} t^{N(L-1)} e^{-NLt} \tag{24}$$

It is worth noting that when $N = 1$, the distribution in Eq. (24) is represented by the speckle model in (4). Accordingly, the higher KS distance (δ_{tr}) between the cumulative distributions model in Eq. (24) and the empirical CDF of T_N estimated over a collection of samples can indicate the heterogeneous regions in the ratio image (*i.e.* the trace image of the ratio matrix). Therefore, the following empirical sigmoid function is proposed to map the parameter δ_{tr} to β_2

$$\beta_2 = \frac{1}{1 + e^{-20(\delta_{tr} - 0.5)}} \tag{25}$$

D. Summary of the Proposed Approach

The implementation process of the proposed framework is summarized in the following algorithms. The proposed algorithm will be defined as Model frEe dEnoising algoriThm for SAR images (MEET-SAR)

Algorithm 1: MEET-SAR Single Channel Data

```
Set the value of the patch size and generate the 4 directional patches.
for all the pixels with coordinates p
    for all the pixels q in the search window
        for all the four directions
            Select the patches P and Q
            Generate the vectors a and v using (7) and (8)
            Compute the distances δ̄_a(p,q) and δ̄_v(p,q)
        end for
    Numerically compute the weights w_a(.) and w_v(.)
    Compute the final weight w(.) in (17)
    end for
Compute the estimated value Â(p) in (19)
Compute the bias reduction as in (21)
end for
```

Algorithm 2: MEET-SAR Multi-Channel Data

```
Set the value of the patch size, generate the 4 directional patches and compute the Ĉ using L neighborhood pixels.
for all the pixels with coordinates p
    for all the pixels q in the search window
        for all the four directions
            Select the patches P and Q
            Generate the vectors a and v using (13) and (16)
            Compute the distances δ̄_a(p,q) and δ̄_v(p,q)
        end for
    Numerically compute the weights w_a(.) and w_v(.)
    Compute the final weight w(.) in (17)
    end for
Compute the estimated value R̂(p) in (18)
Compute the bias reduction as in (20)
end for
```

V. Experimental Results

The capability of the proposed non-local denoising framework in dealing with different SAR image products (Amplitude, Polarimetric, InSAR, PolInSAR) was evaluated and compared with two of the most competitive generic approaches in the literature, *i.e.* NLSAR [21] and Refined Lee (RLee) [36], both of which are able to deal with all the products considered (single image, interferometric images, polarimetric, ...). Moreover, for a further evaluation of MEET-SAR, the comparison with a specifically designed and effective filter is provided for each case of the considered product. In particular, in the case of the single-channel amplitude image, the comparison with NoLAnD [26] is performed; for the polarimetric dataset, the intensity-driven adaptive neighborhood (IDAN) [37] filter is considered; for the InSAR dataset, the recently proposed data-driven Φ-Net algorithm [38] is implemented; finally, for PolInSAR data, the boxcar filter is tested.

Tests were performed on X-, C-, and L-band data acquired from various high-resolution (HR) satellite and aerial sensors. The NL methods were implemented with a patch size of 11×11 pixels and the search window with a size of 19×19 pixels.

The first dataset was acquired by the TerraSAR-X sensor over the city of Tehran, Iran, in the area of the Azadi Complex stadium in 2013, with the system operating in strip-map mode. The spatial resolution of the image is 1.2×6.6 m in range and azimuth directions, respectively. A subset of the SLC image in HH polarization with the size of 250×400 pixels is selected. The corresponding amplitude image is shown in Fig. 3(a).

The second dataset refers to the polarimetric L-band images acquired with the DLR ESAR sensor over the Oberpfaffenhofen test site in Germany. The image resolution is 3×3 m and a subset of data with size 900×700 pixels is selected. The amplitude image in HH polarization, as well as the Pauli image are shown in Fig. 4 (a) and Fig. 5 (a).

The third dataset refers to fully polarimetric C-band images

This article has been accepted for publication in a future issue of this journal, but has not been fully edited. Content may change prior to final publication. Citation information: DOI 10.1109/TGRS.2021.3127109, IEEE Transactions on Geoscience and Remote Sensing

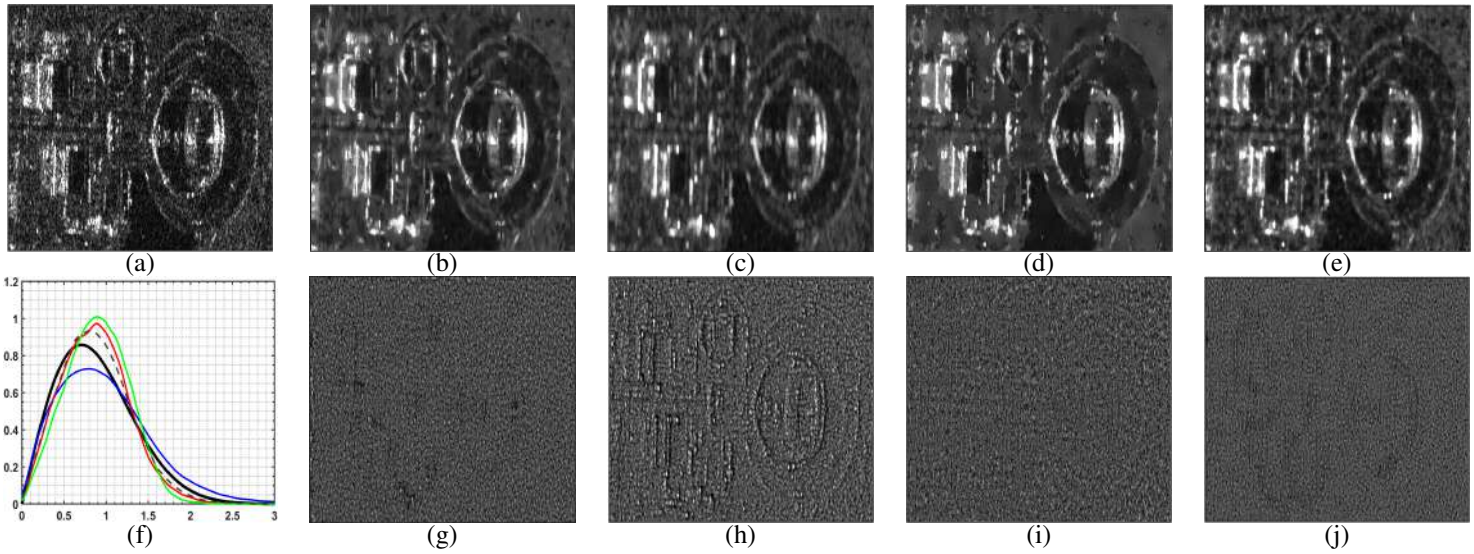

Fig. 3. Single channel despeckling operations on Tehran test site, X-band. **First row:** (a) original SLC amplitude image, filtered images by (b) NoLAnD, (c) RLee, (d) NLSAR, (e) MEET-SAR. **Second row:** (f) Overlapping of the theoretical expected pdf (black solid line) and of the ratio pdfs estimated from NoLAnD (dash gray), RLee (blue), NLSAR (red), MEET-SAR (green) solutions; ratio images produced by (g) NoLAnD, (h) RLee, (i) NLSAR, and (j) MEET-SAR.

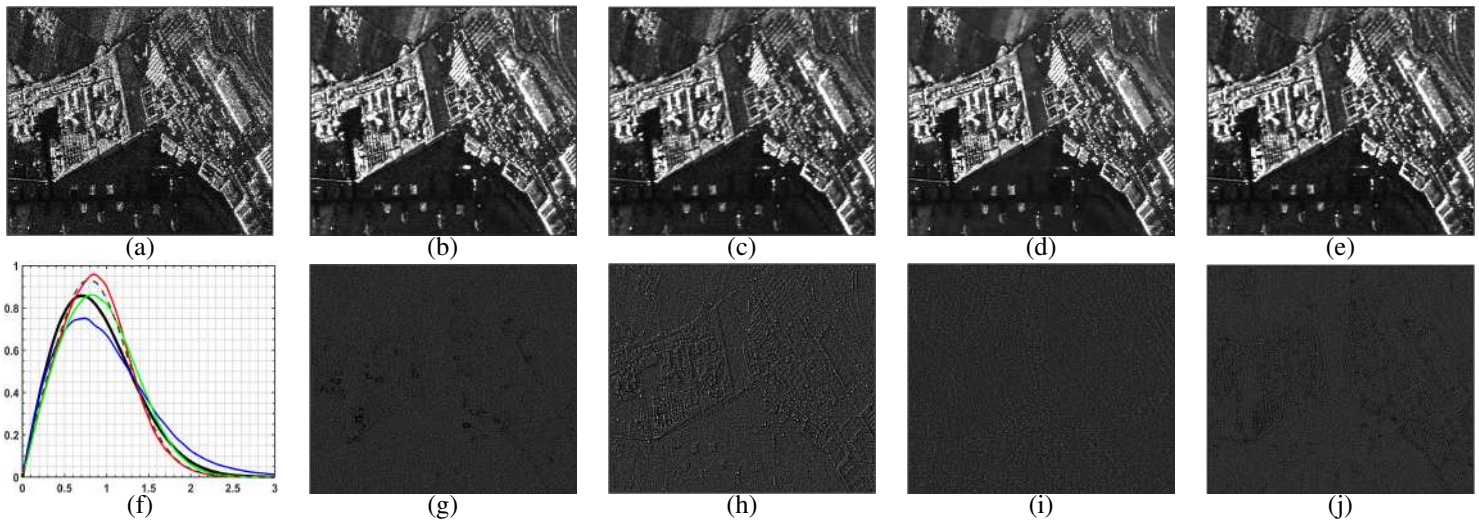

Fig. 4. Single channel despeckling operations on Oberpfaffenhofen test site, L-band. **First row:** (a) original SLC amplitude image, filtered images by (b) NoLAnD, (c) RLee, (d) NLSAR, (e) MEET-SAR. **Second row:** (f) Overlapping of the theoretical expected pdf (black solid line) and of the ratio pdfs estimated from NoLAnD (dash gray), RLee (blue), NLSAR (red), MEET-SAR (green) solutions; ratio images produced by (g) NoLAnD, (h) RLee, (i) NLSAR, and (j) MEET-SAR.

in the Flevoland agricultural area in the Netherlands. The data were acquired by Radarsat-2 in April 2009, with a spatial resolution of 4.7×4.8 (azimuth, range). The image was released by the Canadian Space Agency (CSA). The selected subset of an image consists of 800×600 pixels and contains numerous plant species grown in large rectangular fields, as shown in the Pauli image in Fig. 7 (a). The fourth dataset is an interferometric pair images related to Phoenix, USA. It is a 3 m resolution image acquired with the C-band Radarsat-2 system in HH polarization. The size of the image is 800×1000 pixels and the corresponding interferometric phase is shown in Fig. 9 (a). Finally, for the last test site, the polarimetric interferometric dataset of E- SAR L-band dual-baseline images over the city of Dresden in Germany was used. The Pauli RGB image referenced to the master image of the study area and is shown in Fig. 10 (a). The image size is 562×301 pixels, the spatial resolutions are 3.0 m in azimuth and 2.2 m in range direction.

A. Single channel experiments

In this subsection, the evaluation of the proposed approach is performed using the single-channel amplitude image. The evaluations were performed using the images of Tehran and Oberpfaffenhofen study areas, both in HH polarization. The quantitative assessments are given by the M-index (Mi) [39], β index [40], and the mean (μ) preservation. Typically, the M-index evaluates speckle removal ability along with detail removal aspect [39], [41]. Ideal filters have an M-index equal to 0. The β index computes the correlation between the edges of the original image and the edges in the denoised image,

This article has been accepted for publication in a future issue of this journal, but has not been fully edited. Content may change prior to final publication. Citation information: DOI 10.1109/TGRS.2021.3127109, IEEE Transactions on Geoscience and Remote Sensing

TABLE I
QUANTITATIVE ANALYSES OF DESPECKLING FILTER WITH SINGLE CHANNEL IMAGES

	Tehran				Oberpfaffenhofen			
	μ	β-index	Mi	$SQI\%$	μ	β-index	Mi	$SQI\%$
NOLAND	183.10	0.9982	0.2108	**93.96**	0.0482	**0.9222**	**0.0858**	92.50
RLee	**165.71**	0.9418	**0.0288**	**91.93**	**0.0427**	0.9115	0.1635	92.72
NLSAR	178.25	**0.9989**	0.3747	91.74	0.0462	**0.9991**	0.1778	**94.41**
MEET-SAR	**177.23**	**0.9992**	**0.1337**	86.81	**0.0455**	0.9834	**0.0930**	**94.18**

both of which are detected using the Laplacian filter (or the Canny filter) [40]. The β index ranges from 0 to 1, with a value of 1 representing ideal edge preservation. As for the μ value, it should not change compared to the original image. In addition to the previous indices, the statistical quality index (*SQI*) proposed in [34] is considered. In particular, the quality index evaluates the statistical similarity of the ratio between the original and the filtered images (or covariance matrices, in the case of multiple images) with the properties derived from the pure speckle model. In the case of an ideal filter, its value should tend towards 1 (or towards 100%), as in [34]).

Fig. 3 shows the results of the filtering approaches used for the amplitude image of the first test site (Azadi Stadium in Tehran). From the visual comparison, it can be seen that the image restored by NLSAR is affected by an oversmoothing effect in homogeneous regions (top right of Fig. 3 d). In the results of MEET-SAR, NOLAND and RLee, this problem is handled correctly (Fig. 3 b, c and e). For further evaluation, the ratio images are estimated and shown in the second line of Fig. 3. In general, for an ideal filter, only speckle should remain in the ratio image. From the visual comparison, the structures are visible in the ratio image generated by RLee. Moreover, some spot structures remained in the ratio image of NOLAND (Fig. 3 g) due to some oversmoothing in building areas. Approximately the same structures, with some additional details, are visible in the proposed solution. Although in the ratio image of NLSAR (Fig. 3 i), the structures and content are less preserved, the filtered image suffers from the effect of oversmoothing, as mentioned earlier. For further evaluation, the similarity between the pure speckle distribution and the empirical pdf of the ratio images is compared. The estimated pdfs are shown in Fig. 3 (f). As can be seen, the empirical pdfs from all approaches are similar to the expected Rayleigh speckle pdf. In addition, for numerical evaluation, the evaluation indices are given in Table I. In terms of Mi, the best performance is obtained by RLee, followed by MEET-SAR and NLSAR. In terms of *SQI* index, NOLAND shows the best performance with a value of 93%, while MEET-SAR is characterized by a value around 86%. The mean value of the original speckled image is 165.53, and as can be seen in Table I, RLee has the best mean preservation, followed by the proposed approach. Moreover, in terms of β index (Table I), the best performance is obtained with the proposed method and NLSAR, while RLee shows the worst performance.

For more analysis, the second intensity image relating to the Oberpfaffenhofen area (Fig. 4 a) is processed. The restored images of the test site are shown together with their ratio images in Fig. 4. Visual comparison shows that all the approaches

TABLE II
SQI VALUE (IN %) FOR THE POLARIMETRIC DATA

	IDAN	RLee	NLSAR	MEET-SAR
Oberpfaffenhofen	41.12	61.54	61.06	**97.62**
Flevoland	70.02	76.35	69.90	**95.60**

used produce very similar filtered results. As can be seen, the structures are clearly visible in the ratio image obtained with RLee (Fig. 4 h), indicating poor performance of the filtered image in Fig. 4 (c). The oversmoothing effect by NLSAR (Fig. 4 d) in the homogeneous regions (upper left part of the filtered image) can be observed. Instead, visual inspection of the filtered images of the proposed approach (Fig. 4 e) confirms that the result is not affected by any oversmoothing effect in either the building or vegetation regions. However, in the ratio image of the proposed approach (Fig. 4 j), compared to the ratio obtained by NOLAND (Fig. 4 g), more structures can be seen.

The evaluation approach in [34] is used to evaluate the results. The estimated pdfs are shown in Fig. 4 (f). The original noisy image has a mean of 0.0427, while the images filtered with NOLAND, RLee, NLSAR and MEET-SAR have means of 0.0482, 0.0427, 0.0462 and 0.0455, respectively. This again shows that RLee and the proposed method can preserve the best mean value. In addition, for numerical evaluation, the homogeneity index (Mi), the β index as well as the *SQI* are calculated and presented in Table. I. In general, filter ranking by quantitative indices is a problematic task because each index may represent a particular aspect of despeckling efficiency. Looking at the results given in Table I for the indices, all approaches show similar efficiency. MEET-SAR is the second best in terms of the three parameters considered and shows good performance in terms of the different aspects analyzed by the three indices. It is important to highlight a difference between MEET-SAR and NOLAND. Both methods are based on KS distance, but in NOLAND one of the cumulative functions needed for the computation is known analytically. This can lead to a better estimate of the similarity measure, using a limited number of pixels. However, the model assumption of NOLAND may affect the results in the non fully developed speckle areas, such as layovered ones.

B. Polarimetric SAR experiments

After assessing the method on single-channel amplitude images, further evaluation is performed on fully polarimetric datasets . The results are compared with IDAN, RLee [36] and NLSAR approaches [21]. For this purpose, the despeckled polarimetric covariance matrix of the test areas Oberpfaffenhofen

This article has been accepted for publication in a future issue of this journal, but has not been fully edited. Content may change prior to final publication. Citation information: DOI 10.1109/TGRS.2021.3127109, IEEE Transactions on Geoscience and Remote Sensing

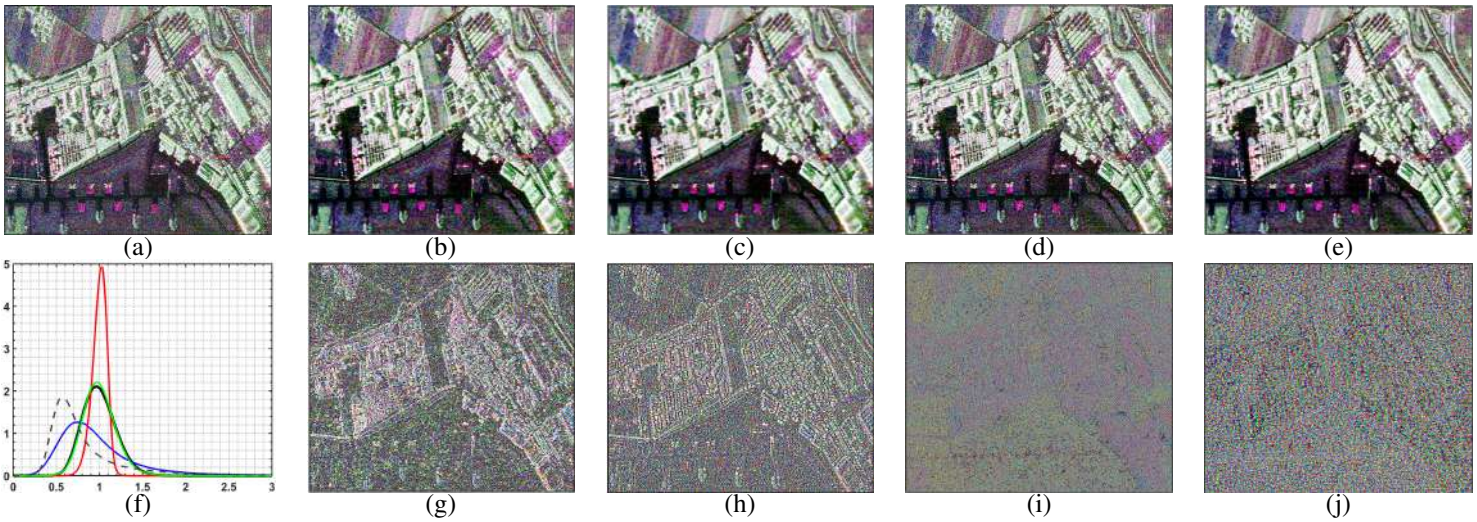

Fig. 5. Results of polarimetric filtering operations in Pauli basis representation on Oberpfaffenhofen test site. **First row:** (a) original SLC amplitude image, filtered images by (b) IDAN, (c) RLee, (d) NLSAR, (e) MEET-SAR. **Second row:** (f) Overlapping of the theoretical expected pdf (black solid line) and of the ratio pdfs estimated from IDAN (dash gray), RLee (blue), NLSAR (red), MEET-SAR (green) solutions; ratio amplitude images provided by (g) IDAN, (h) RLee, (i) NLSAR, and (j) MEET-SAR.

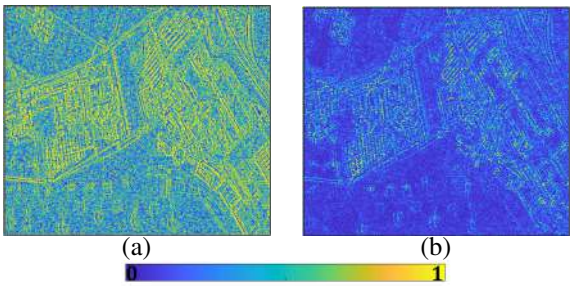

Fig. 6. The estimated β images in the bias reduction step, (a) NLSAR (b) MEET-SAR.

and Flevoland is estimated with the considered approaches. Qualitative evaluation is again performed by visual inspection on the obtained filtered and Pauli colour-coded ratio images.

Figure 5 shows the restored and ratio images of the Oberpfaffenhofen area in Pauli basis color coding. The visual comparison of the filtered images with respect to the original image in Fig. 5(a) confirms that MEET-SAR outperforms the others, both in terms of speckle removal and detail preservation. Furthermore, to verify this, the ratio covariance matrix (or speckle matrix) of each method is given by $\hat{\mathbf{S}} = \boldsymbol{\Sigma}^{\frac{-1}{2}}\mathbf{C}\boldsymbol{\Sigma}^{\frac{-1}{2}}$ and their corresponding Pauli ratio images are shown in the second line of Fig. 5. As mentioned earlier, with effective filtering, only speckle should remain in the ratio image. As shown in Fig. 5 (g) and (h), the structures in the ratio images derived from IDAN and RLee are remained, indicating the poor performance of despeckling filtering. Although NLSAR reduces the geometric content in the ratio image (Fig.5 i), most of the pixels are not filtered properly, which means that the recovered image (Fig.5 d) is still affected by the noise effect. In contrast, in the output of the proposed approach (Fig.5 e), the noise effect is significantly reduced while the edges are preserved (Fig.5 j). The ratio image appears characterized by limited details and an almost homogeneously distributed residual speckle. For the quantitative analysis of the filter performance, the pdfs of the trace of the ratio or speckle matrices are computed and shown in Fig. 5 (f). Under the fully developed speckle model, the trace of the speckle matrix is expected to follow the central Chi-square distribution with $2NL$ degrees of freedom, as shown in (24). The distribution related to MEET-SAR tends to overlap with the expected one (see lines in green and black, respectively). For further assessment, the *SQIs* of [34], are calculated on the ratio matrices and reported in Table II. As can be seen, the results of filter ranking by statistical index are consistent with visual inspection.

To illustrate the difference of MEET-SAR versus NLSAR in the bias reduction step, the estimated β parameters by both approaches are shown in Fig. 6. As can be seen, using the variance-based technique of NLSAR (β_1), a high value of β is estimated even in homogeneous areas (Fig. 6 a), while using the information from the heterogeneity of the ratio image, according to (26), the β value is significantly reduced in such areas. From the evaluation of the results, the noisy recovered image by NLSAR (Fig.5 d) is mainly associated with the poor estimation of the β parameter.

Further experiments on the efficiency of the applied filtering operations using the fully polarimetric dataset are presented with the Flevoland images. The recovered images and the corresponding ratio matrices (computed as for the previous test case) in Pauli color coding representation are computed and shown in Fig. 7 (a). In analogy to the previous experiment, in the filtered images based on IDAN and RLee (Fig. 7 b and c), the edge information is lost due to the oversmoothing effect. This can be verified in the ratio matrix images (Fig. 7 g and h), where several residual details are visible. The results by NLSAR (Fig. 7 d) are strongly affected by the noise effect, which is most likely due to the poor performance of its bias reduction step [21] Moving to the restored image by the proposed technique, the noise is significantly reduced and the edges are preserved (Fig. 7 e): the ratio matrix image again

This article has been accepted for publication in a future issue of this journal, but has not been fully edited. Content may change prior to final publication. Citation information: DOI 10.1109/TGRS.2021.3127109, IEEE Transactions on Geoscience and Remote Sensing

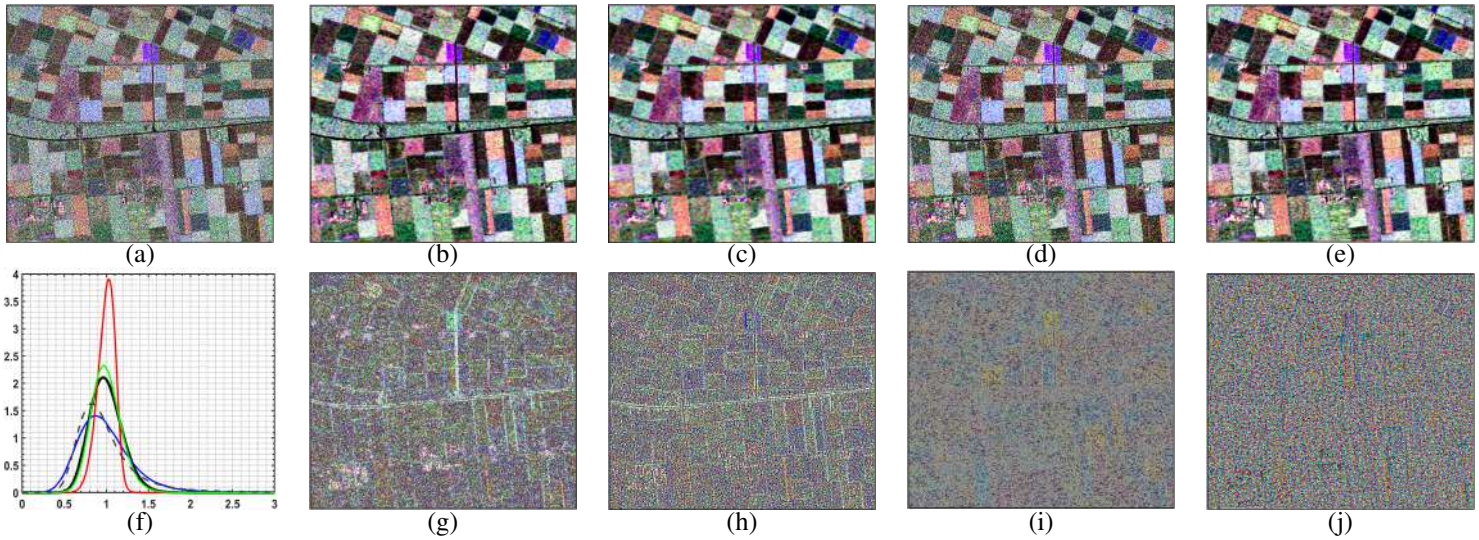

Fig. 7. Results of polarimetric filtering operations in Pauli basis representation on Flevoland test site. **First row:** (a) original SLC amplitude image, filtered images by (b) IDAN, (c) RLee, (d) NLSAR, (e) MEET-SAR. **Second row:** (f) Overlapping of the theoretical expected pdf (black solid line) and of the ratio pdfs estimated from IDAN (dash gray), RLee (blue), NLSAR (red), MEET-SAR (green) solutions; ratio amplitude images provided by (g) IDAN, (h) RLee, (i) NLSAR, and (j) MEET-SAR.

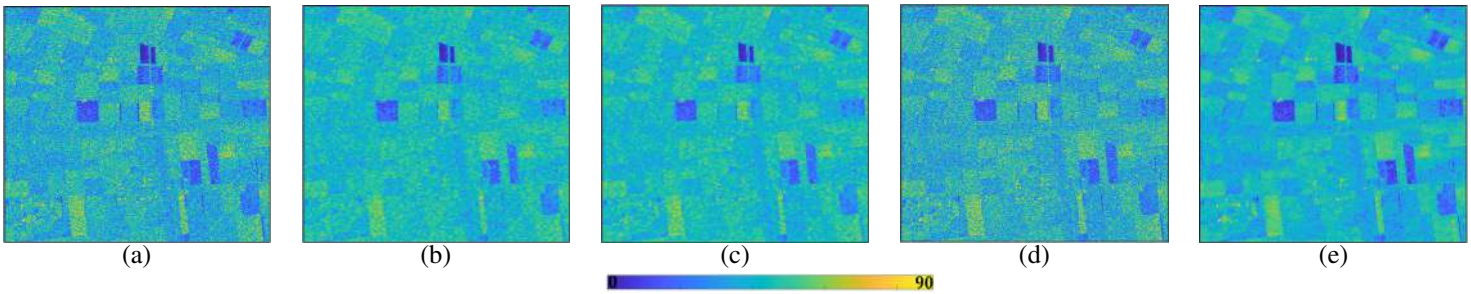

Fig. 8. The estimated α angle ([0-90] *degrees*) from the $H/\alpha/A$ decomposition [33]. (a) original, (b) IDAN, (c) RLee, (d) NLSAR, and (e) MEET-SAR.

shows the good capabilities of the filter (Fig. 7 j). Besides the visual evaluation of the image, the pdfs of the ratio covariance matrices are shown in Fig. 7 (f). Also in this case, the pdf related to MEET-SAR tends to overlap with the expected one, unlike the others. The *SQIs* listed in Table II confirm this point. An additional evaluation is performed with respect to the basic principle of polarimetric SAR data filtering, *i.e.*, the preservation of polarimetric features. For this purpose, the well-known incoherent $H/\alpha/A$ decomposition [33] was performed and Fig. 8 shows the estimated α angle from the original and filtered datasets. From the estimated polarimetric α angle, the consistency between all filtered approaches and the original one (Fig. 8 a) is confirmed. However, the estimated α image from the proposed filtering approach enjoys speckle suppression and edge preservation. It should be noted that experiments for entropy and anisotropy images (not reported here for brevity) have shown similar results.

C. Interferometric SAR experiments

In this subsection, the performance of the proposed approach in estimating interferometric phase and coherence images is evaluated. The test is conducted on a hilly area around Phoenix, USA, described at the beginning of this section. For comparison, the results of the data-driven Φ-Net algorithm [38] and two generic algorithms, RLee and NLSAR, are shown in Fig. 9. From the qualitative comparison of the phase and coherence images, and in analogy with the previous experiments from polarimetric data, the results from NLSAR still suffer from the noise effect (Fig. 9 d and n). However, moving to the Φ-Net result and the proposed approach, the noise effect is significantly reduced. The interferometric phase image of Φ-Net is properly denoised, while some details are lost and smoothing effect is enforced by this data-driven approach. Refined Lee preserves the details and avoids strong smoothing, however the performance of this approach is affected by undesirable fluctuations in the phase values due to non-optimal noise composition. In contrast, the proposed approach avoids smoothing while preserving details and properly removing noise effects. Moving to the coherence, the good performances of Φ-Net and MEET-SAR are evident, compared to the initial coherence image, estimated with $L = 1$ (Fig. 9 (k)). The latter is very noisy and its high values in terms of visualization are mainly related to the noise effect, which need be removed by spatial averaging using filtering techniques.

Further evaluation is performed by estimating the phase difference image obtained by subtracting the filtered phase image from the noisy original image in Fig. 9(a). In the case

This article has been accepted for publication in a future issue of this journal, but has not been fully edited. Content may change prior to final publication. Citation information: DOI 10.1109/TGRS.2021.3127109, IEEE Transactions on Geoscience and Remote Sensing

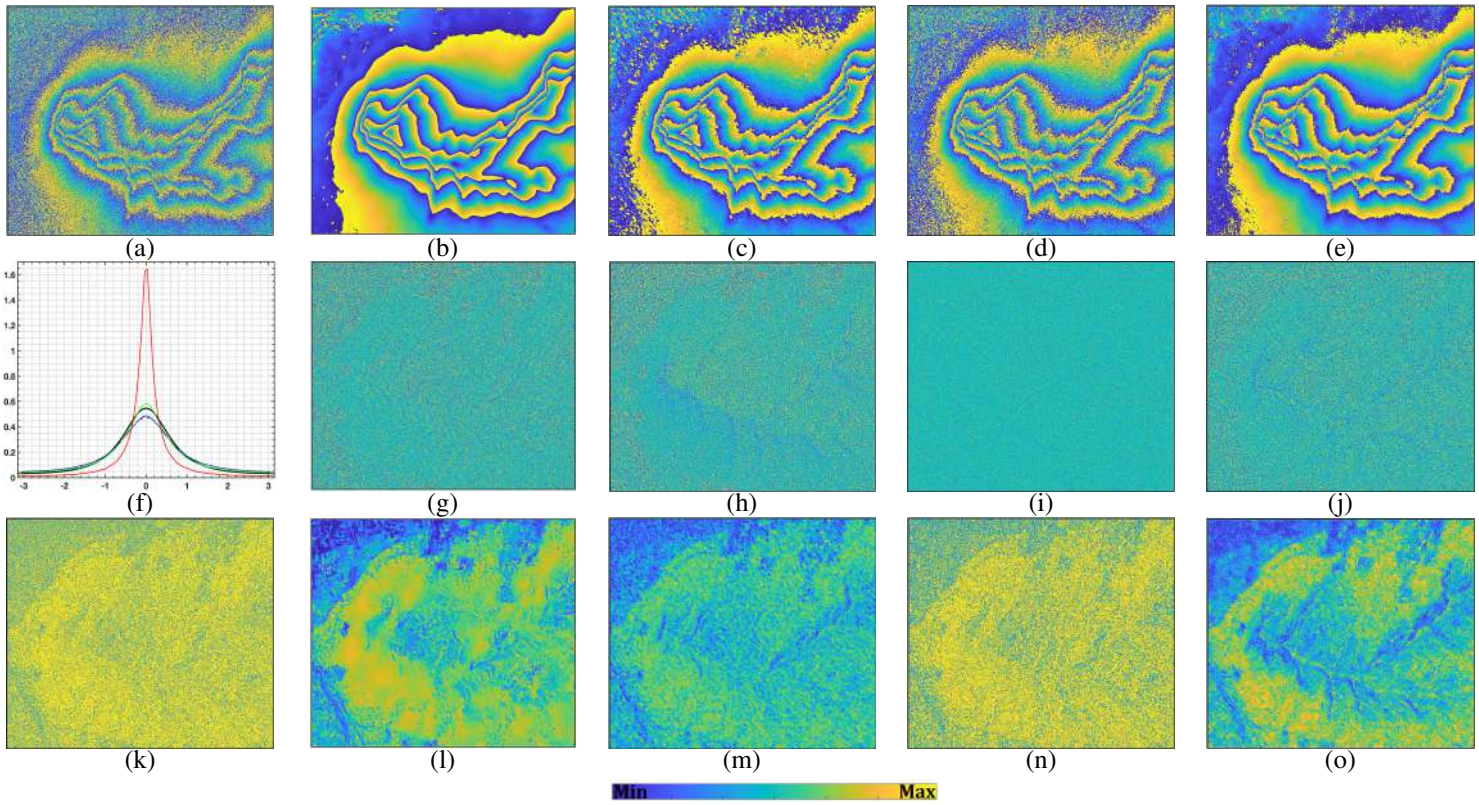

Fig. 9. Results of interferometric filtering operations on Phoenix test site. **First row:** (a) original interferometric phase image, filtered images by (b) Φ-Net, (c) RLee, (d) NLSAR, (e) MEET-SAR; all images are shown in the interval $[-\pi\ \pi]$. **Second row:** (f) Overlapping of the theoretical expected pdf (black solid line) and of the phase difference pdfs estimated from Φ-Net (dash gray), RLee (blue), NLSAR (red), MEET-SAR (green) solutions; phase difference images, shown in the interval $[-\pi\ \pi]$, produced by (g) Φ-Net, (h) RLee, (i) NLSAR, (j) MEET-SAR. **Third row:** (k) original coherence image, estimated coherence images by (l) Φ-Net, (m) RLee, (n) NLSAR, and (o) MEET-SAR; all images are shown in the interval [0 1].

of an ideal filter, the difference image should not contain any details and should be characterized only by random noise following the distribution of the interferometric phase noise, as described in [42]. From the inspection of the difference image, the good performance of MEET-SAR is evident. The plots of the pdfs related to the phase difference images are estimated and shown in Fig. 9 (f). The pdfs are computed on a region of interest (ROI) without residual fringes, characterized by a nearly homogeneous coherence value. To evaluate the goodness of the pdfs, we have given the theoretical pdf of the interferometric noise [42] computed with the mean coherence value of the selected ROI. From the plot, the most similar pdf to the theoretical one is obtained by the MEET-SAR. In this case, as mentioned in Table III the *SQI* values are 89.93%, 89.91%, 67.61%, and 92.97% for the case of data-driven Φ-Net, RLee, NLSAR and. MEET-SAR, respectively.

In addition, the performance of filtering to reduce the number of residues in the generated interferograms is evaluated [43]. The total number of residues in the unfiltered interferogram is 58253 and filtering reduces the residues significantly as shown in Table III. Comparison of the results shows that the Φ-Net approach best reduces the residues in the filtered interferogram. However, the performance of this data-driven approach in terms of preserving statistical properties is lower than that of our proposed method. MEET-SAR is a model-free approach that is able to preserve the main statistical

TABLE III
QUANTITATIVE EVALUATION OF DESPECKLING FILTERS WITH INSAR DATASET

	Φ-Net	RLee	NLSAR	MEET-SAR
SQI index	89.93	89.91	67.61	92.97
Number of phase residues	228	1477	15708	2031

characteristics of SAR data after filtering based on the given *SQI* values in Table III. Finally, it should be noted that *SQI* is estimated over a homogenous area, while the residues are computed on the whole image. Thus, the *SQI* provides information about the goodness of the filter on area where no discontinuities or coherence changes are present. This explains the different behaviours of the filters in terms of two indexes.

D. Polarimetric-interferometric (PolInSAR) SAR experiments

This experiment is devoted to the evaluation of MEET-SAR for filtering the PolInSAR dataset. For this purpose, the fully polarimetric dual-baseline images in the Dresden test area are considered. In addition to the RLee and NLSAR filters, MEET-SAR is also compared with the widely used boxcar solution for this test case. The results of the applied filtering in estimating the covariance matrix are shown in Fig. 10 by indicating the Pauli image of the master polarimetric dataset and the corresponding ratio matrix image. In addition, the

This article has been accepted for publication in a future issue of this journal, but has not been fully edited. Content may change prior to final publication. Citation information: DOI 10.1109/TGRS.2021.3127109, IEEE Transactions on Geoscience and Remote Sensing

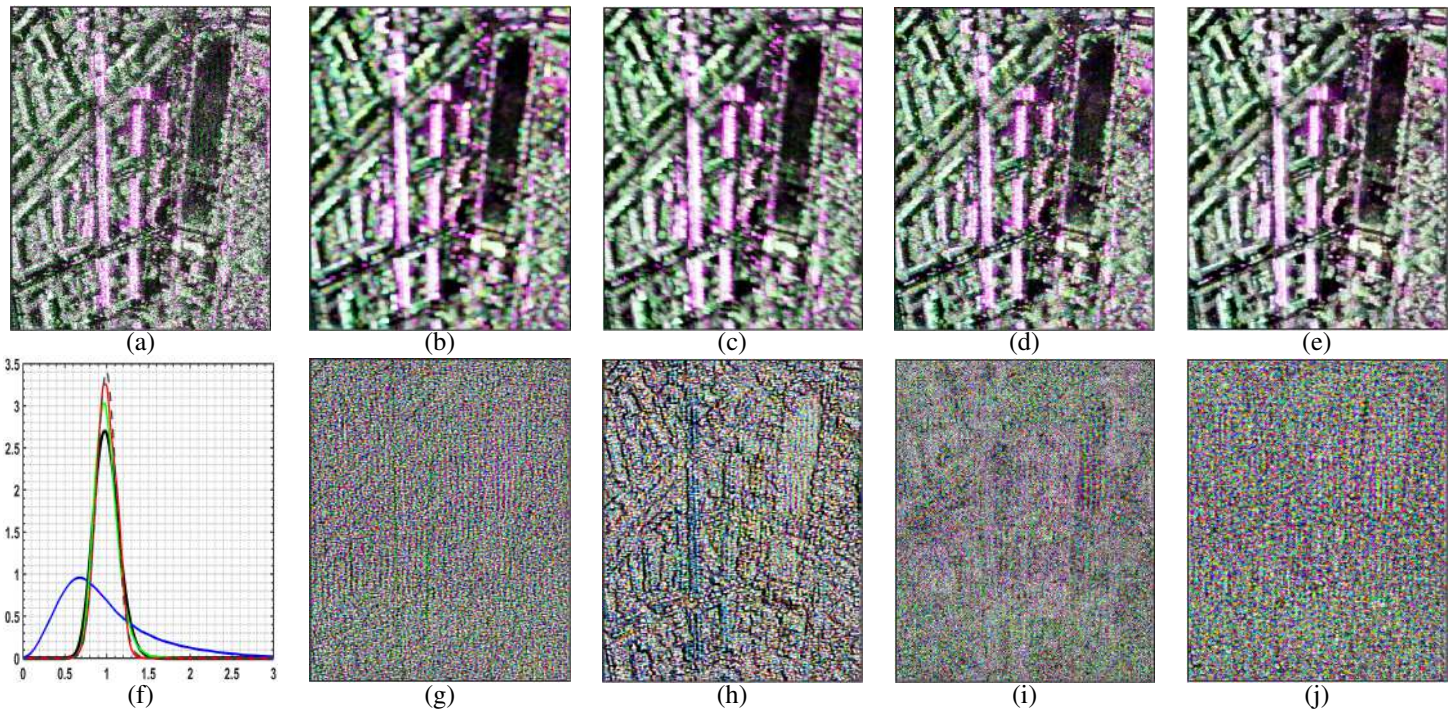

Fig. 10. Results from PolINSAR filtering operations on Dresden test site. **First row:** Pauli image of the master (a) original data and of the filtered ones by (b) boxcar, (c) RLee, (d) NLSAR, (e) MEET-SAR. **Second row:** (f) Overlapping of the theoretical expected pdf (black solid line) and of the ratio covariance matrices pdfs estimated from boxcar (blue), RLee (dash gray), NLSAR (red) and MEET-SAR (green) solutions; ratio covariance matrices provided by (g) boxcar, (h) RLee, (i) NLSAR, and (j) MEET-SAR.

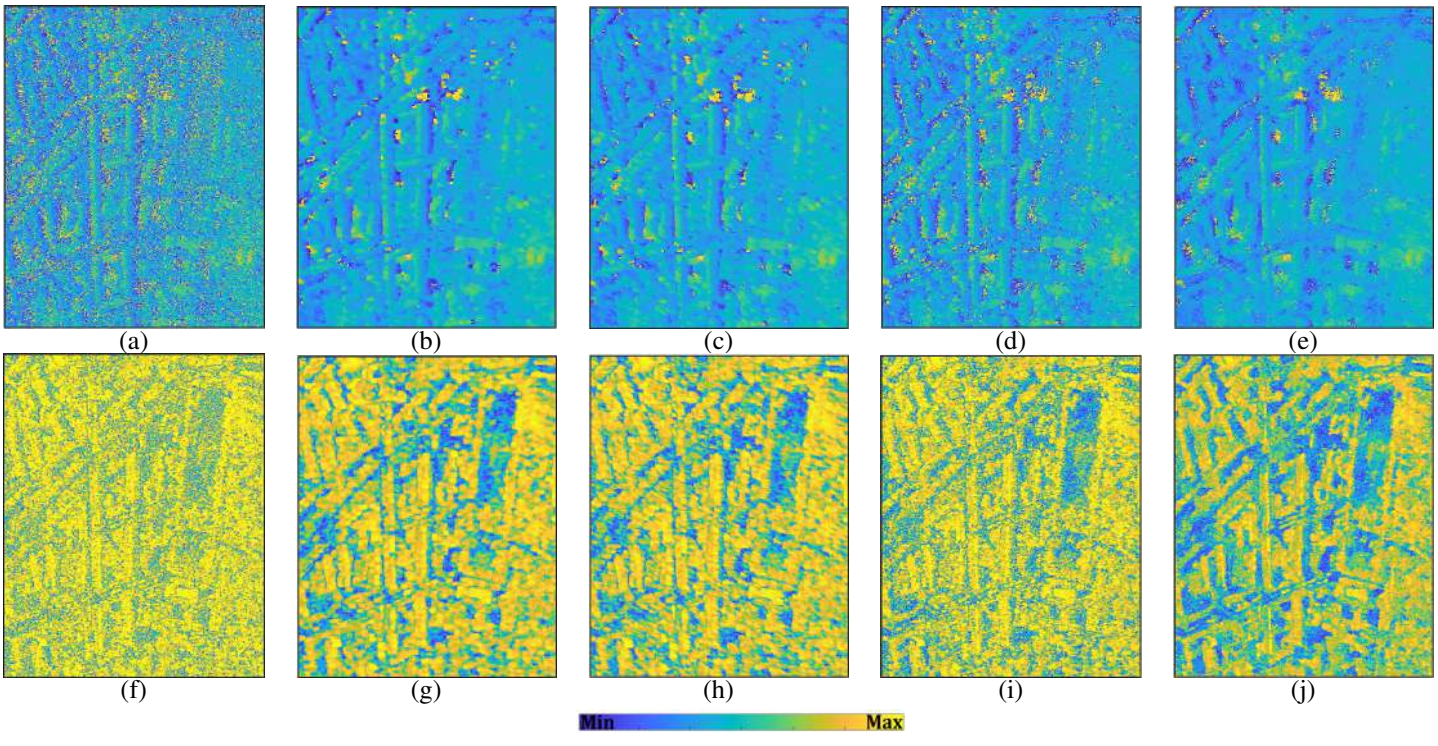

Fig. 11. Results from PolINSAR filtering operations on Dresden test site. **Frst row:** HV interferometric phase image ($[-\pi\ \pi]$) of the (a) original data and of the filtered ones by (b) boxcar, (c) RLee, (d) NLSAR, (e) MEET-SAR. **Second row** VV channel coherence ($[0\ 1]$) of the (f) original data and of the filtered ones by (g) boxcar, (h) RLee, (i) NLSAR, (j) MEET-SAR

interferometric phase between the first and third images in HV polarization and the coherence image in VV polarization are shown in Fig. 11.

From the visual evaluation of the Pauli images (the first row of Fig. 10), it appears that speckle is well suppressed by Boxcar, RLee and the proposed approaches. However, the first two techniques are characterized by the oversmoothing effect (Fig. 10 c and d), while MEET-SAR maintains a good performance in terms of resolution loss (Fig. 10 e and j). The ratio matrix image of NLSAR confirms that urban pixels are still affected by speckle (Fig. 10 i). It should be noted that the implementation of NLSAR with a higher patch or window size or the implementation without bias reduction may provide a better speckle suppressed image, while for the sake of fair comparison, both non-local approaches were processed under the same conditions and with the same window (19×19) and patch (11×11) sizes. From the interferometric phase images (first row of Fig.11) and the coherence images (second row of Fig.11), the oversmoothing effect by traditional Boxcar and RLee is evident. The details are better preserved by NLSAR, while MEET-SAR outperforms the others in terms of speckle suppression and edge preservation.

The effectiveness of MEET-SAR is mainly due to the definition of model-free similarity criteria, which allows it to cope with the limitation of model-based techniques in heterogeneous and mixed scenarios, as in this test case. In addition, the technique has an optimal bias-reduction step that provides the ability to recover the bright pixels while keeping the speckle effect low. The quantitative evaluation of the estimated PolInSAR ratio covariance matrices is performed by the statistical pdfs shown in Fig. 10 (f). Also for this case, the pdf of MEET-SAR has the largest overlap compared to the expected one. The *SQIs* computed for the considered filters are 88.52%,42.58%, 89.51%, and 94.46% for the case of the boxcar, the refined Lee, the NLSAR, and the MEET-SAR, respectively. Therefore, in both visual inspection and statistical analysis, the better rank of the filters used was obtained by MEET-SAR.

VI. Conclusion

In this paper, a generic non-local methodology for despeckling a variety of SAR products, from a single image to polarimetric and interferometric data, has been presented. The strength aspect of the proposed approach relates to the definition of model-free similarity criteria that can handle different SAR modalities, and it is independent of the number of look, noise correlation or model assumptions for the observed scenario. Moreover, the framework uses the heterogeneity information of the ratio image to refine the filtered image in the bias reduction step. The additional main features of the developed and implemented framework relate to the use of anisotropy for similarity assessment. The proposed algorithm is completely unsupervised concerning the tuning of the parameters. The framework has been tested on different datasets using SAR images acquired in different configurations including single channel amplitude images, polarimetric data and polarimetric-interferometric images. The obtained results have shown the effectiveness of the proposed method. The algorithm is able to suppress the speckle while preserving the details and avoiding oversmoothing. The analyses of the experimental results have confirmed the effectiveness of MEET-SAR in both homogeneous and inhomogeneous urban areas, without being concerned about the speckle model. In particular, the experimental analyses showed that the proposed method outperformed the other generic filters (RLee, NLSAR), while its performance was comparable to those of the specially designed algorithms (NoLAnD, IDAN, Φ-Net), making the proposed algorithm a useful generic tool for the recovery of SAR products. Moreover, it is important to note that, although it was not investigated in this study, the proposed framework can handle covariance matrix estimation from a large number of interferometric time-series datasets. In such a case, the commonly adapted GLR-based similarity cannot be efficient because the number of samples for the pre-estimation of the covariance matrix is much smaller than the dimensionality of the stack data vector, which leads to the invalidity of the Wishart distribution model. Finally, it should be noted that the denoising performance achieved by the proposed method comes at the cost of high computational cost. The computational cores of the proposed method are mainly related to 1) the multiplication of complex matrices and matrix inverse and 2) the empirical pdf estimation from the generated data vectors. In the case of single-channel data, the proposed method requires additional estimation of the empirical pdf compared to NoLAnD, since in NoLAnD one of the pdfs to be compared is known from the model assumption. This may in fact duplicate the computational process of MEET-SAR with respect to NoLAnD. In the case of multi-channel data, the proposed method with respect to NLSAR involves matrix inversion, matrix multiplication, and trace and empirical pdf estimation, which can significantly increase the computational cost. The higher runtime may limit the application of the proposed method, but some tips can be considered to reduce the processing time. For example, the running time of the code can be reduced by using Matlab Mex files or by using parallel computing and Graphics Progressing Units (GPUs).

Acknowledgments

The authors thank the German Aerospace Center (DLR), the European and Canadian Space Agencies for for providing the employed datasets.

References

[1] N. R. Goodman, "Statistical analysis based on a certain multivariate complex gaussian distribution (an introduction)," *The Annals of mathematical statistics*, vol. 34, no. 1, pp. 152–177, 1963.

[2] A. Moreira, P. Prats-Iraola, M. Younis, G. Krieger, I. Hajnsek, and K. P. Papathanassiou, "A tutorial on synthetic aperture radar," *IEEE Geoscience and Remote Sensing Magazine*, vol. 1, no. 1, pp. 6–43, 2013.

[3] J. Lee, "Digital image enhancement and noise filtering by use of local statistics," *IEEE Transactions on Pattern Analysis and Machine Intelligence*, vol. PAMI-2, no. 2, pp. 165–168, March 1980.

[4] D. T. Kuan, A. A. Sawchuk, T. C. Strand, and P. Chavel, "Adaptive noise smoothing filter for images with signal-dependent noise," *IEEE Transactions on Pattern Analysis and Machine Intelligence*, vol. PAMI-7, no. 2, pp. 165–177, March 1985.

[5] R. Touzi, A. Lopes, and P. Bousquet, "A statistical and geometrical edge detector for sar images," *IEEE Transactions on Geoscience and Remote Sensing*, vol. 26, no. 6, pp. 764–773, Nov 1988.

[6] G. Franceschetti, V. Pascazio, and G. Schirinzi, "Iterative homomorphic technique for speckle reduction in synthetic-aperture radar imaging," *Journal of the Optical Society of America A: Optics and Image Science, and Vision*, vol. 12, no. 4, pp. 686–694, 1995.

[7] F. Argenti and L. Alparone, "Speckle removal from sar images in the undecimated wavelet domain," *IEEE Transactions on Geoscience and Remote Sensing*, vol. 40, no. 11, pp. 2363–2374, 2002.

[8] F. Argenti, A. Lapini, T. Bianchi, and L. Alparone, "A tutorial on speckle reduction in synthetic aperture radar images," *IEEE Geoscience and remote sensing magazine*, vol. 1, no. 3, pp. 6–35, 2013.

[9] R. Touzi, "A review of speckle filtering in the context of estimation theory," *IEEE Transactions on Geoscience and Remote Sensing*, vol. 40, no. 11, pp. 2392–2404, 2002.

[10] T. T. Lê, A. M. Atto, E. Trouvé, and J. Nicolas, "Adaptive multitemporal sar image filtering based on the change detection matrix," *IEEE Geoscience and Remote Sensing Letters*, vol. 11, no. 10, pp. 1826–1830, 2014.

[11] D. Coltuc, E. Trouve, F. Bujor, N. Classeau, and J. P. Rudant, "Time-space filtering of multitemporal sar images," in *IGARSS 2000. IEEE 2000 International Geoscience and Remote Sensing Symposium. Taking the Pulse of the Planet: The Role of Remote Sensing in Managing the Environment. Proceedings (Cat. No.00CH37120)*, vol. 7, 2000, pp. 2909–2911 vol.7.

[12] R. Touzi and A. Lopes, "The principle of speckle filtering in polarimetric sar imagery," *IEEE Transactions on Geoscience and Remote Sensing*, vol. 32, no. 5, pp. 1110–1114, 1994.

[13] C. Lopez-Martinez and X. Fabregas, "Model-based polarimetric sar speckle filter," *IEEE Transactions on Geoscience and Remote Sensing*, vol. 46, no. 11, pp. 3894–3907, 2008.

[14] J. Lee, T. L. Ainsworth, Y. Wang, and K. Chen, "Polarimetric sar speckle filtering and the extended sigma filter," *IEEE Transactions on Geoscience and Remote Sensing*, vol. 53, no. 3, pp. 1150–1160, 2015.

[15] A. Arienzo, F. Argenti, L. Alparone, and M. Gherardelli, "Accurate despeckling and estimation of polarimetric features by means of a spatial decorrelation of the noise in complex polsar data," *Remote Sensing*, vol. 12, no. 2, 2020.

[16] A. C. Frery, H. . Muller, C. C. F. Yanasse, and S. J. S. Sant'Anna, "A model for extremely heterogeneous clutter," *IEEE Transactions on Geoscience and Remote Sensing*, vol. 35, no. 3, pp. 648–659, May 1997.

[17] C. Tison, J. M. Nicolas, F. Tupin, and H. Maître, "A new statistical model for Markovian classification of Urban areas in high-Resolution SAR images," *IEEE Transactions on Geoscience and Remote Sensing*, vol. 42, no. 10, pp. 2046–2057, 2004.

[18] C.-A. Deledalle, L. Denis, and F. Tupin, "Iterative weighted maximum likelihood denoising with probabilistic patch-based weights," *IEEE Transactions on Image Processing*, vol. 18, no. 12, pp. 2661–2672, 2009.

[19] S. Parrilli, M. Poderico, C. V. Angelino, and L. Verdoliva, "A nonlocal sar image denoising algorithm based on llmmse wavelet shrinkage," *IEEE Transactions on Geoscience and Remote Sensing*, vol. 50, no. 2, pp. 606–616, Feb 2012.

[20] H. Feng, B. Hou, and M. Gong, "Sar image despeckling based on local homogeneous-region segmentation by using pixel-relativity measurement," *IEEE Transactions on Geoscience and Remote Sensing*, vol. 49, no. 7, pp. 2724–2737, 2011.

[21] C. Deledalle, L. Denis, F. Tupin, A. Reigber, and M. Jäger, "Nl-sar: A unified nonlocal framework for resolution-preserving (pol)(in)sar denoising," *IEEE Transactions on Geoscience and Remote Sensing*, vol. 53, no. 4, pp. 2021–2038, April 2015.

[22] W. Zhao, C. Deledalle, L. Denis, H. Maître, J. Nicolas, and F. Tupin, "Ratio-based multitemporal sar images denoising: Rabasar," *IEEE Transactions on Geoscience and Remote Sensing*, vol. 57, no. 6, pp. 3552–3565, 2019.

[23] A. Mazza, F. Sica, P. Rizzoli, and G. Scarpa, "Tandem-x forest mapping using convolutional neural networks," *Remote Sensing*, vol. 11, no. 24, 2019. [Online]. Available: https://www.mdpi.com/2072-4292/11/24/2980

[24] X. Ma and P. Wu, "Multitemporal sar image despeckling based on a scattering covariance matrix of image patch," *Sensors*, vol. 19, no. 14, 2019.

[25] L. Torres, S. J. S. Sant'Anna, C. da Costa Freitas, and A. C. Frery, "Speckle reduction in polarimetric sar imagery with stochastic distances and nonlocal means," *Pattern Recognit.*, vol. 47, pp. 141–157, 2013.

[26] G. Ferraioli, V. Pascazio, and G. Schirinzi, "Ratio-based nonlocal anisotropic despeckling approach for sar images," *IEEE Transactions on Geoscience and Remote Sensing*, vol. 57, no. 10, pp. 7785–7798, Oct 2019.

[27] D. Yue, F. Xu, A. C. Frery, and Y. Jin, "A generalized gaussian coherent scatterer model for correlated sar texture," *IEEE Transactions on Geoscience and Remote Sensing*, vol. 58, no. 4, pp. 2947–2964, 2020.

[28] J. W. Goodman, "Some fundamental properties of speckle," *JOSA*, vol. 66, no. 11, pp. 1145–1150, 1976.

[29] C. A. Deledalle, L. Denis, G. Poggi, F. Tupin, and L. Verdoliva, "Exploiting patch similarity for sar image processing: The nonlocal paradigm," *IEEE Signal Processing Magazine*, vol. 31, no. 4, pp. 69–78, July 2014.

[30] C.-A. Deledalle, L. Denis, and F. Tupin, "How to compare noisy patches? patch similarity beyond gaussian noise," *International journal of computer vision*, vol. 99, no. 1, pp. 86–102, 2012.

[31] A. L. R. Touzi and P. Bousquet, "A statistical and geometrical edge detector for sar images," *IEEE Transactions on Geoscience and Remote Sensing*, vol. 26, no. 6, pp. 764–773, 1988.

[32] J.-S. Lee, "Speckle analysis and smoothing of synthetic aperture radar images," *Computer graphics and image processing*, vol. 17, no. 1, pp. 24–32, 1981.

[33] J.-S. Lee and E. Pottier, *Polarimetric radar imaging: from basics to applications*. CRC press, 2009.

[34] H. Aghababaei and G. Ferraioli, "Statistical indices for despeckling evaluation in multichannel sar images," *IEEE Geoscience and Remote Sensing Letters*, pp. 1–5, 2020.

[35] L. Wei, O. Tirkkonen, P. Dharmawansa, and M. McKay, "On the exact distribution of the scaled largest eigenvalue," in *2012 IEEE International Conference on Communications (ICC)*, June 2012, pp. 2422–2426.

[36] J.-S. Lee, "Refined filtering of image noise using local statistics," *Computer graphics and image processing*, vol. 15, no. 4, pp. 380–389, 1981.

[37] G. Vasile, E. Trouve, Jong-Sen Lee, and V. Buzuloiu, "Intensity-driven adaptive-neighborhood technique for polarimetric and interferometric sar parameters estimation," *IEEE Transactions on Geoscience and Remote Sensing*, vol. 44, no. 6, pp. 1609–1621, 2006.

[38] F. Sica, G. Gobbi, P. Rizzoli, and L. Bruzzone, "Φ-net: Deep residual learning for insar parameters estimation," *IEEE Transactions on Geoscience and Remote Sensing*, vol. 59, no. 5, pp. 3917–3941, 2021.

[39] L. Gomez, R. Ospina, and A. Frery, "Unassisted quantitative evaluation of despeckling filters," *Remote Sensing*, vol. 9, no. 12, p. 389, 2017.

[40] L. Gomez, M. E. Buemi, J. C. Jacobo-Berlles, and M. E. Mejail, "A new image quality index for objectively evaluating despeckling filtering in sar images," *IEEE Journal of Selected Topics in Applied Earth Observations and Remote Sensing*, vol. 9, no. 3, pp. 1297–1307, 2016.

[41] S. Vitale, D. Cozzolino, G. Scarpa, L. Verdoliva, and G. Poggi, "Guided patchwise nonlocal sar despeckling," *IEEE Transactions on Geoscience and Remote Sensing*, vol. 57, no. 9, pp. 6484–6498, Sep. 2019.

[42] G. Fornaro and V. Pascazio, "Chapter 20 - sar interferometry and tomography: Theory and applications," in *Academic Press Library in Signal Processing: Volume 2*. Elsevier, 2014, vol. 2, pp. 1043–1117.

[43] H. Yu, Y. Lan, Z. Yuan, J. Xu, and H. Lee, "Phase unwrapping in insar : A review," *IEEE Geoscience and Remote Sensing Magazine*, vol. 7, no. 1, pp. 40–58, 2019.

Hossein Aghababaei (M'16, SM'2020) received the M.Sc. degree in remote sensing from the University of Tehran, Tehran, Iran, in 2012 and the Ph.D. degree in synthetic aperture radar (SAR) remote sensing from K. N. Toosi University of Technology, Tehran, in 2017. From 2017 to 2019, he was a research fellow at Telecommunication Group, Università degli Studi di Napoli Parthenope. Currently, he is an Assistant Professor at the University of Twente, Faculty of Geo-Information Science and Earth Observation (ITC), Enschede, the Netherlands. His research interests are polarimetric and multichannel SAR image processing, radar interferometry and tomography. He is also associate editors of IEEE Geoscience and Remote Sensing Letters and MDPI Remote Sensing.

Giampaolo Ferraioli (SM'17) was born in Lagonegro, Italy, in 1982. He received the BS and MS degrees and the Ph.D. degree in Telecommunication Engineering from the Università degli Studi di Napoli Parthenope in 2003, 2005 and 2008, respectively. He has been Visiting Scientist at Département TSI of Télécom ParisTech, Paris, France. Currently, he is an Assistant Professor with Università degli Studi di Napoli Parthenope. His main research interests deal with Statistical Signal and Image Processing, Radar Systems, Synthetic Aperture Radar Interferometry, Image Restoration and Magnetic Resonance Imaging. In 2009 he won the "IEEE 2009 Best European PhD Thesis in Remote Sensing" prize, sponsored by IEEE Geoscience and Remote Sensing Society. He serves as Associate Editor of IEEE Geoscience and Remote Sensing Letters and he is in the Editorial Board of MDPI Remote Sensing. He is member of the Technical Liaison Committee for IEEE Transactions on Computational Imaging.

Sergio Vitale (S' 18) received the MS degree in telecommunication engineering (summa cum laude) from Università degli Studi di Napoli Federico II, Napoli, Italy, in 2017. He received the Ph.D degree in Information and Communication Technology and Engineering from Università degli Studi di Napoli Parthenope 2021. He is currently a Post Doctoral researcher with Università degli Studi di Napoli Parthenope. He serves as Associate Editor of MDPI Sensors. His research interests include synthetic aperture radar imaging, image enhancement, super-resolution, and deep learning

Roghayeh Zamani received the MS degree in Geodesy and Geomatics Engineering from K. N. Toosi University of Technology, Tehran in 2019. She was employed as a research assistant at Università degli Studi di Napoli Parthenope in 2021. She is currently a PhD student at the University of Twente, Faculty of Engineering Technology (ET), Enschede, the Netherlands. Her research interests are synthetic aperture radar interferometry and time series analysis for remote sensing based hazard mapping.

Gilda Schirinzi (M'14, SM'17) received the M.Sc. degree in electronic engineering from the University of Naples Federico II, Napoli, Italy, in 1983. She joined the Electronic Engineering Department, University of Naples Federico II, as a Research Fellow. From 1985 to 1986, she was with European Space Agency, ESTEC, The Netherlands. In 1988, she joined the Istituto di Ricerca per l'Elettromagnetismo e i Componenti Elettronici (IRECE), Italian National Council of Researches, Napoli. In 1992, she was appointed the Head of the Electromagnetics Division, IRECE, and in 1997, she became a Senior Researcher. In 1998, she joined the University of Cassino, Cassino, Italy, as an Associate Professor of Telecommunications. In 2005, she became a Full Professor. Since 2008, she has been with the Telecommunication Group, University of Naples "Parthenope," Napoli. She has taught signal theory, electrical communications, microwave remote sensing systems, and image processing. Her research interests include SAR signal processing and coding, SAR interferometry and tomography, microwave imaging techniques, and image and signal processing for remote sensing applications

Vito Pascazio (SM'11) graduated summa cum laude in electronic engineering from the Università di Bari, Bari, Italy, in 1986. In 1990, he received the Ph.D. degree in Electronic Engineering and Computer Science from the Department of Electronic Engineering, Università di Napoli Federico II, Napoli, Italy. In 1990, he was at the Research Institute on Electromagnetics and Electronic Devices (IRECE), Italian National Council of Research (CNR), Napoli, Italy. Currently, he is a Full Professor and Chair of the Department of Engineering at the Università di Napoli Parthenope, Napoli, Italy. From 1994 to 1995, he was a Visiting Scientist at the Laboratoire des Signaux et Systemes of the Ecole Superieure d' Electricite (Supelec), Gif sur Yvette, France, and from 1998 to 1999, with the Universite de Nice Sophia-Antipolis, Nice, France. He was also Director of National Laboratory of Multi-Media Communications of the Italian Consortium of Telecommunications (CNIT), Napoli, Italy. He has published more than 180 technical papers. His research interests include Remote Sensing, Image processing, and Linear and Non-Linear estimation, with particular emphasis to Image Computing and Processing, and Reconstruction of Microwave and Radar images. Dr. Pascazio was awarded the Philip Morris Prize for Scientific and Technological Research, in 1990. He was a General Co-Chairman of IGARSS-2015 conference.